Weather and Climate Extremes 33 (2021) 100331

Contents lists available at ScienceDirect

Weather and Climate Extremes

journal homepage: www.elsevier.com/locate/wace

# Observation and modeling of Hurricane Maria for damage assessment

Rabindra Pokhrel [a,*], Salvador del Cos [a], Juan Pablo Montoya Rincon [a], Equisha Glenn [a], Jorge E. González [a,b]

[a] Department of Mechanical Engineering, USA
[b] NOAA-CREST Center, The City College of New York, NY, 10031, USA

ARTICLE INFO

*Keywords:*
Hurricane Maria
Observation and modelling
WRF
Precipitation
Orographic effect
Damage assessment

ABSTRACT

The human loss due to Hurricane Maria (H-Maria) in the month of September of 2017 was quantified to be more than 4500 casualties in the entire island of Puerto Rico, making it the most devastating storm in US history. Besides, H-Maria left a lasting impact on the Island as it brought to full collapse the electrical power grid rendering the Island entirely out of power for more than ten months. The aim of this work is to fill the gap of the hydro-meteorological processes of this relevant storm due to the limited observational data available. The synoptic observational record shows that the monthly average Sea Surface Temperature of 30 °C, with an anomaly of 0.5 °C as well as low vertical wind shear of 4–8 m/s fueled H-Maria. Simulated (WRF) time series of wind speed is in close resemblance compared with the limited data available from ocean buoys with a simulated and observed peak wind speed of 30 m/s on the southern coast of the Island. The total rainfall for the event was simulated to peak at 762 mm (observed 965 mm) at the center of the Island and was validated with post-hurricane National Weather Service (NWS) rainfall with a Normalized Root Mean Square Error (RMSE) of 0.2. The orographic effects are simulated, reflecting enhancement of the rainfall at high altitudes in the central mountains of the Island. As an example of damage assessment, the risk of failure of the electrical power towers as a function of wind speed and soil saturation is simulated using statistical models for the entire Island, which results in higher risks of failure at the Northwest and center of the Island. These validated results of the storm can also be used as an input for other analysis such as hydrological models to geo-locate regions for risks due to flooding.

## 1. Introduction

Hurricane Maria (H-Maria) made landfall on the southeast coast of Puerto Rico on September 20, 2017, as an intense Category 4 hurricane. The long-term average of Tropical cyclone (T.C.) landfall events in the northern Caribbean, close to Puerto Rico, is once per year (Pielke et al., 2003). The National Hurricane Center Report (NHC 2019) on Maria highlights it as the strongest Hurricane to make landfall on the island since 1928. H-Maria broke rainfall records that resulted in unprecedented flooding and mudslides and combined with sustained winds of 69.3 m/s (155 MPH), where the rainfall had a storm total of 965 mm (38 inches) (NHC 2019) that contributed to a near-complete loss of the electrical grid and municipal water supplies for the 3.4 million residents (Pasch et al., 2018). All physical infrastructure was affected with 80% destruction of electrical power and communication transmission systems, including utility poles and cellular towers, and ultimately the storm resulted in an estimated cost of 90 billion ($USD) in damage between Puerto Rico and the U.S. Virgin Islands, which exceeds the previously costliest storm to affect Puerto Rico directly, Hurricane Georges in 1998, by 85 billion dollars (Pasch et al., 2018). The mortality study found the death toll related to the storm more than 70 times the official estimate of 64 counts bringing the total count to 4645 (Kishore et al., 2018).

The United States Geological Survey(USGS), Cooperative Observer Program (COOP), the Caribbean Regional Association for Coastal Ocean Observing(CARICOOS), and the National Climatic Data Center (NCDC) have historical data recorded from 1995 to 2017 covering the entire island. The WSR-88D NEXRAD station in Puerto Rico has a relatively small amount of data for the event as it ceased operations during H-Maria at 10:00 a.m. GMT on September 20. When compared to other intense storms, H-Maria was an exceptional event when it comes to maximum and total rainfall. H-Maria had a maximum recorded rainfall

* Corresponding author.
*E-mail address:* rabindra@ku.edu.np (R. Pokhrel).

https://doi.org/10.1016/j.wace.2021.100331
Received 28 December 2020; Received in revised form 8 May 2021; Accepted 17 May 2021
Available online 20 May 2021

that was determined to have a return period of 115 years for the entire island and 152 years in smaller regions within the island. (Keellings and Hernández-Ayala, 2019). There are many factors affecting event rainfall throughout the island, especially given the interaction of the orographic effects from the mountains, a process that has been studied in very limited basis, and there is a possibility that it contributed more towards the rainfall totals when compared to other hurricanes (Colón-Pagán et al., 2009). This, in addition to the previously discussed data, it shows that Maria was a significant outlier.

The underlying factors for the long-term trends in tropical Atlantic warmth and tropical cyclone activity is the increase in sea surface temperatures (SST), which are related to anthropogenic activity and greenhouse gases manifested in a global warming (Mann et al., 2006). The SSTs in the Caribbean have been increasing over the past 35 years (1980–2015) (Glenn et al., 2015) and it is projected to further increase (Jury., 2011). Furthermore, NOAA reports that 2017 was the hottest year on record at the time, for land and ocean surface temperatures without the El Nino boost (NOAA, 2017). SSTs are not the single key variable affecting hurricanes (Henderson-Sellers et al., 1998; Holland, 1997; Emanuel, 1999). Other factors may include amplified high-pressure ridge in the upper troposphere across the central and eastern North Atlantic (Chelliah. et al., 2004), reduced vertical wind shear (Henderson-Sellers et al., 1998) over the central North Atlantic and African easterly lower atmospheric winds, and atmospheric stability (Tang. et al., 2004) which favors the development of hurricanes. As there are many variables to fuel the storm, it is essential to understand the common synoptic and local conditions to anticipate the storm's strength. In this study, we discuss two synoptic variables SST and vertical wind shear during H-Maria.

The ability to anticipate the damage that a storm will likely cause is a research area that has been getting attention as a predictive indicator of damage to aid in better preparing and respond to disasters. The main impact a tropical storm could have can be essentially distilled into three categories: wind, landslides, and flooding both coastal and inland. With the documented rise of SST, higher intensity storms become more frequent and more powerful (Bjarnadottir et al., 2013). It thus becomes more important to quantify the impacts caused by these storms.

In Puerto Rico during H-Maria, the extreme conditions by the storm caused the electric power infrastructure to fail to full collapse. Failures of parts of the electrical system due to storms are not uncommon, and there have been detailed studies on the statistical failure of wooden power poles under changing climate conditions (Bjarnadottir et al., 2013). Larger scale impact assessments have been done in test cases to make a probabilistic assessment of an entire power infrastructure system and how to improve its damage resiliency on the multi-regional scale (Panteli et al., 2017). Statistical models for future scenarios are not ignored either, as models have shown an increase of wind speed intensity will be in general experienced in the future on the Northeastern Coast of the U.S. (Mudd et al., 2014; Comarazamy et al., 2020).

Winds also impact the forest canopy and, in historical studies, it has been shown that using the Fujita damage rating one can go back in history and estimate the general strength of a hurricane by analyzing some of the damage caused to the forest canopy (Boose et al., 2004). In this case, F2 (Extensive tree blowdowns) and F3 (Most trees are downed) are of interest because those levels are where the forest canopy gets damaged. Historical records reported that an F3 event hits western Puerto Rico every 150 years and Eastern Puerto Rico every 50, forming a gradient (Boose et al., 2004). Recent study analyzes and reflects in the impacts of changes in forest canopy in convective activity and precipitation prior and after H-Maria (Hosannah et al., 2020). One of the more dangerous effects of hurricanes for coastal areas is the storm surge as the storm causes the local sea level to rise and severely damage the local area. A storm in 1970 in Bangladesh with a storm surge of 10.6 m killed 300,000 people, after which the government began to build shelters to help reduce the casualties, and the risk areas were identified using computer simulations (Karim and Mimura, 2008). A hybrid statistical/deterministic approach to identifying future storm surge events have been used in New York City by making synthetic tracks over the Atlantic Ocean and recording the results while comparing them to real life (N. Lin et al., 2010a,b). Determining where landslides occur is not a simple task as there are a large number of factors that are needed to determine including topography, vegetation, and water saturation, and rainfall to be able to predict future landslides (Philpott et al., 2008).

In order to use these experiences as learning events for damage assessment on the society and the infrastructure, reliable metrological variables are required at high temporal and spatial scales across the islands. This by itself is a challenging task for H-Maria as the National Weather Service (NWS) NEXRAD collapsed in the first hours of the storm. In this research, we use the Weather Research and Forecast (WRF) model, a non-hydrostatic model that works well on the mesoscale level (ten to a few hundred kilometers) that allows for the physical representation of cloud radiation processes and planetary boundary layer dynamics throughout all of the assigned vertical levels and has been used for Hurricane modeling in a number of cases (Zhang and Villarini et al., 2018; Patricola et al., 2018; Davis et al., 2008a; Khain et al., 2010; Chen et al., 2011; Moon and Nolan 2015). This modeling tool has been used to determine that flooding was exacerbated by urbanization during hurricane Harvey in the Gulf of Mexico in 2017, delineating how the effects of urbanization contributed to higher di-adiabatic heating, which in turn fed the storm (Zhang and Villarini et al., 2018). WRF has also been used to estimate the relative strength of various storms, including H-Maria, in various future scenarios to simulate anthropogenic climate change to estimate how high SST would affect storm strength (Patricola et al., 2018). In this research, H-Maria is simulated in WRF, and the outputs of the models (at 1-km spatial and 1-h temporal resolution) are compared and validated with the limited observational records available for storm tracks, rainfall, and wind speed. The model outputs are used to understand the vertical and horizontal movement that enhanced the precipitation at the mountain range. The output was further utilized to assess the damage on the electric power poles.

## 2. Methods

### 2.1. Recreating Hurricane Maria with WRF simulation

This study employs a single-layer urban canopy version of WRF v 3.8.1 model (Skamarock et al., 2008), a numerical weather prediction system developed by the National Center for Atmospheric Research (NCAR). WRF is well suited for this study due to three main reasons. First, lateral boundary conditions allow us to conduct a two-way nesting permitting an interaction between the outer and inner simulations domain. It also allows us to prescribe a tighter constraint on large scale circulations of the tropical cyclone than if a global model were used (Patricola et al., 2018). This is suitable because the simulations to reproduce hurricane track, maximum winds, and precipitations are sensitive to underlying SST and the surrounding environmental conditions. Second, WRF uses a non-hydrostatic approximation to solve vertical momentum equations, whereas the global model uses simplified hydrostatic approximation. Third, the regional domain allows us to perform ensembles of simulations at convection-permitting resolution (less than 3 km as WRF can resolve convective process explicitly at these resolutions), which would be computationally less feasible with a global model.

Three two-way nested domains were used for domain configuration. The parent domain of 25 km (144 points by 100 points) contains the entire Mesoamerican and Caribbean region. The second domain contains the Caribbean Sea, Dominican Republic, and the island of Puerto Rico at a spatial resolution of 5 km (306 points by 191 points), and the third domain contains the entire island of Puerto Rico at a spatial resolution of 1 km (336 points by 156 points). The domain configuration is presented in Fig. 1 (left panel), whereas Fig. 1 (right panel) also shows

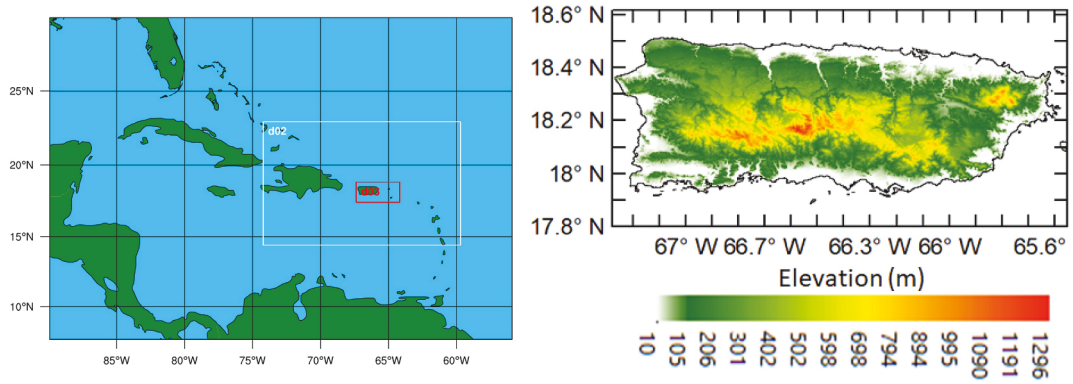


**Fig. 1.** WRF domain (d01-50km, d02-25km and d03-1km) and Elevation for finer domain.

the smallest domain with elevation contours. The center of the island contains the mountain range with elevation as high as 1300 m. The cumulus parameterization was turned off for the 1 km domain, as WRF can resolve convective processes explicitly at this resolution. There are 50 vertical levels, with 35 of them below 2 km height. The simulation was conducted for four days from September 18 to September 22, 2017. The spin-off period of 12 h is selected to capture the event. The results for finer one km domain and a temporal resolution of 1 h for rainfall and winds is used in the analysis.

To resolve the interaction between the land surface and the atmosphere, the Noah land surface model (Tewari et al., 2004) is used. The Noah land surface model employs land use classes to determine the thermal, radiative, and hydrological properties of the land surface. The model was configured to use the rapid radiative transfer model for longwave radiation (Mlawer et al., 1997), the Dudhia scheme for short wave radiation (Dudhia 1989), Yonsei University Scheme (YUS) for Planetary Boundary layer, the Kain-Fritsch cumulus parameterization (Kain and Kain 2004) and the WSM6 microphysics (S.-Y. Hong and Lim 2006). These parameterizations (Table 1) discussed above were used following recommendations on hurricane simulation in WRF user guide developed by NCAR (http://www2.mmm.ucar.edu/wrf/users/).

A list of seven ensembles (Table 2) was chosen based on the initial and boundary conditions (four) and different planetary boundary layer (PBL)-YUS (S. Y. Hong, Noh, and Dudhia 2006), MYNN- (Nakanishi and Niino, 2004, 2006), and for cumulus parameterizations Kain et al. (2004) and Zhang et al. (2011) were used to find the storm track that resembles closer to the observation. Four of those ensembles were focused on input data (1. NCEP, 2. NCEP-FNL, and 3. NCEP CFSv2 (Saha et al., 2014) reanalysis, and 4. NCEP CFSv2 forecast). The other three ensembles mainly cover changing PBL and cumulus parameterization. The NCEP CFSv2 with above parameterization (Table 1) resulted in the best track and is in close resemblance with the observation record and outputs from this ensemble is used in the entire analysis. The CFSv2 (as compared to other inputs like NCEP and NCEP-FNL) is able to capture the storm more closely to NHC observation record maybe mainly due to the low resolution of the CFSv2 input data. In addition, the normalized root mean square error for this simulation for total storm precipitation is much lower (0.2) than other simulations.

**Table 1**
WRF parameterization.

| WRF Parameterization | |
|---|---|
| Microphysics | WRF Single-Moment 6-class scheme (Hong and Lim 2006) |
| Longwave Radiation | RRTM (Mlawer et al., 1997) |
| Land Surface | Noah Land Surface Model (Tewari et al., 2004) |
| Planetary Boundary Layer | Younsei University Scheme (Hong et. 2006) |
| Cummulus Parameterization | Kain-Fritsch cumulus parameterization, used only for coarser domain (Kain and Kain 2004) |

**Table 2**
Eight ensemble experiments conducted to find a better hurricane track.

| Ensemble | Representation |
|---|---|
| NCEP_1 | (No Storm) |
| NCEP_FNL | NCEP_FNL |
| CFSv2_MYNN (PBL) | CFSv2_PBL |
| CFSv2_YUS (PBL)+Kain(CU) | CFSv2 |
| CFSv2_Zhang(CU) | CFSv2_Cumulus |
| CFSv2_Zhang(CU)+MYNN(PBL) | CFSv2_Combined |
| CFSv2_Forecasat + YUS(PBL)+Kain(CU) | CFSv2_Forecast |
| CFSv2_Reanlysis_No height | CFSv2_No Height |

### 2.2. Risk of failure of the electrical distribution poles

Using WRF meteorological data and mechanical stress analysis approximations, and the electrical distribution of poles with design criteria, the risk of failure for a distribution line pole was determined. First for the dimensions and maximum admissible load are selected as Class 5 pole (American National Standards Institute (ANSI., 2002), as a result of Puerto Rico Electric Power Authority reporting that 85% of the transmission lines are built to less than a Class 4 criteria (Group, 2017). The ANSI classification of wood poles is presented in Table 3. The Southern Pine is one of the most common materials used to build electric power utility poles across the US (Wolfe and Moody, 1997). Therefore, it was selected as the pole material for the risk assessment.

To determine when the pole will fail, we considered the effect of all the loads that are perturbing the system. In other words, the bending moment due the wind in the pole ($M_p$) and conductors ($M_w$), and the bending moment due to the conductors tension ($M_t$). Moreover, the maximum bending moment in the pole will be the sum of all previously

**Table 3**
ANSI classification of wood poles (American national standards institute (ANSI) 2002).

| Pole class | Horizontal Load (N) | Length range (m) | Minimum tip circumference (m) |
|---|---|---|---|
| H5 | 44,480 | 13.7–38.1 | 0.94 |
| H4 | 38697.6 | 12.2–38.1 | 0.89 |
| H3 | 33360 | 12.2–28.1 | 0.84 |
| H2 | 28467.2 | 10.7–28.1 | 0.79 |
| H1 | 24019.2 | 10.7–28.2 | 0.74 |
| 1 | 20016 | 10.7–28.3 | 0.69 |
| 2 | 16457.6 | 6.1–38.1 | 0.64 |
| 3 | 13344 | 6.1–27.4 | 0.58 |
| 4 | 10675.2 | 6.1–21.3 | 0.53 |
| 5 | 8451.2 | 6.1–15.2 | 0.48 |
| 6 | 6672 | 6.1–13.7 | 0.43 |
| 7 | 5337.6 | 6.1–10.7 | 0.38 |
| 9 | 3291.52 | 6.1–9.1 | 0.38 |
| 10 | 1645.76 | 6.1–7.6 | 0.30 |

calculated moments (Lee Layton, 2017).

$$M_{Max} = M_p + M_t + \sum (M_w WS)$$

Where, $WS$ is the distance between poles (Conductor length).

The strength of the pole is given by the fiber stress (Property of the material, $F_s$) and the diameter in the ground line ($C_{gnd}$) (Keshavarzian 2003). To find the permissible bending moment at the ground line we use the following correlation:

$$M_r = 0.000264 * F_s * C_{gnd}$$

Mechanical failure of the pole is considered when the maximum bending moment is larger than the permissible. Furthermore, we are also considering the pole stability as a different kind of failure, when the pole is able to withstand the load, but the soil is not generating enough resistance to keep the pole attached then the pole is considered to have failed too. The pole stability is given by an empirical correlation that is directly dependent on the height ($H_{pole}$) and setting depth ($D$) of the pole, and the soil moisture ($S_e$).

$$M_{soil} = \left[S_e * D^{3.75} / \left(H_{pole} - 0.0662 * D\right)\right] * \left(H_{pole} - D\right)$$

The pole is considered to fail by stability when the maximum bending moment is larger than the soil permissible bending moment ($M_{soil}$). As an example, a pole will be considered failed if $M_{soil} > M_{Max} > M_r$ (failure by bending moment) or $M_r > M_{Max} > M_{soil}$(failure by stability)

The risk will be estimated as following: High risk, we will consider the resistance of a pole class 4, $M_r$ = 1321.5 kN m; Medium risk, will consider the resistance of a pole class 5, $M_r$ = 1058.1 kN m; Low risk means that none of the poles will fail. A Failure by stability$M_{soil}$, will be considered high risk as well.

## 3. Results

### 3.1. Synoptic conditions during hurricane Maria

Previous reports indicate the SSTs during 2017 were some of the warmest on record (NOAA, 2017), and the Caribbean region was no exception. Using NOAA's Optimum Interpolation Sea Surface Temperature (OISST) analysis product, results show that sea surface temperature anomalies of the Caribbean region for September (1982–2018) were as high as 0.50 °C without an El Nino signal, as seen in Fig. 2 (Reynolds et al., 2007). The spatial plot on Fig. 2 shows that SSTs anomalies for September for the Caribbean region were as high as 0.57–0.89 °C. Hurricane activity generally occurs over the oceans in regions where SSTs exceed 26 °C (Henderson-Sellers et al., 1998). In the Atlantic, SSTs and hurricane activity vary widely on inter-annual and multi-decadal time scales. One factor in the year-to-year variability is El Niño: Atlantic hurricanes are suppressed when an El Niño is underway in the Pacific (Gray 1984; Tang et al., 2004). Fig. 2 observed that September 2017 was one of the hottest September in the record without El Nino boost in SSTs (Kalnay et al., 1996).

In addition to high SSTs, low vertical wind shear, lower than 8 m/s (Paterson et al., 2005), also helps in hurricane formation and intensification (i.e., the wind shear tends to inhibit the vortex from forming). For the entire Caribbean region, climatological records show that vertical wind shear (VWS, the difference between 850 and 200 hPa wind speed) for July, August, and September are lower than 10 m/s (Fig. 3) and are the months when hurricanes are likely to occur in the region. The spatial plot of Fig. 3 delineates the region with VWS contours along with the shaded contours of SST and hurricane tracks for three different hurricanes that passed through the same region during September 2017. Low VWS of 4 m/s was observed, 50% less than the climatology (Fig. 3) wind shear of 8 m/s during the same month of Hurricane Maria. In addition to low vertical wind shear, high SST of 30–31 °C (spatial plot of Fig. 3) is observed southwest of the Caribbean region. Ocean cooling (difference of ~4 °C) is observed to exist in the northeast of the region that follows the hurricane path and is attributed to high wind speed and precipitation along the path.

### 3.2. Comparison of modeling results with observation

The simulated minimum Sea Level Pressure (SLP) for each ensemble component is shown in Fig. 4 and compares well with the observation from the National Hurricane Center (NHC). The CFSv2 reanalysis initialization tracks the storm closer to the NHC record than the forecast, NCEP, and NCEP-FNL. The same simulation also shows that the storm made landfall at the southeast of the island with a wind speed of 60 m/s and leaves the island northwest at a speed of 52 m/s.

In addition to the comparison of storm track with NHC, the NEXRAD Radar data for 1-h precipitation just before the landfall is compared with WRF simulation results for three time periods for September 20, 2017. The top panel of Fig. 5 is the NEXRAD radar precipitation, whereas the bottom panel is WRF simulation results. Both panels show the landfall at a similar location with similar magnitude. The Radar data at 9:50 a.m. GMT indicates the rain band with curved orientation and similar orientation is seen in WRF simulation. WRF results have a lag of 3 h and have an elongated eye as compared to the observation. However, the magnitude and the orientation of the storm is seen to be captured by the model.

Fig. 6 (left) is presented with the locations of the CARICOOS buoys (for sub-hourly wind speed) along the coast, the cooperative stations (COOP), NCDC, and USGS stations for precipitation along with the location of the NEXRAD radar. The wind speed's temporal variation for four different locations is also shown in Fig. 6 (right panel). For Mayaguez (west), the maximum wind speed for both the observation and model output is seen to peak at 25 m/s. Wind speed is in close resemblance compared with the limited data available from ocean buoys with

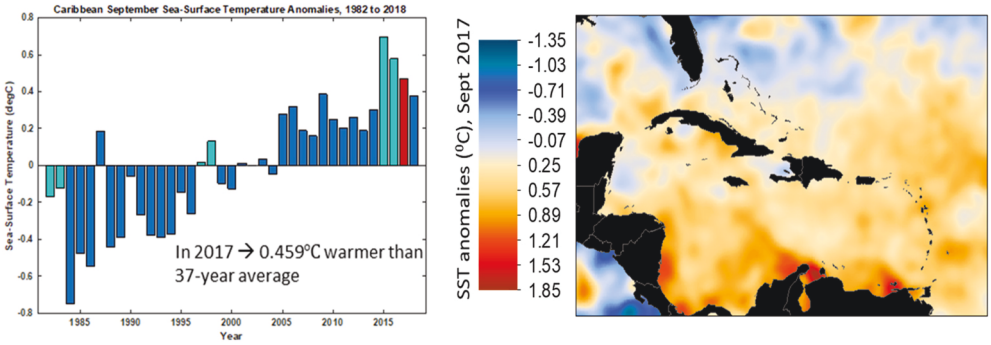


**Fig. 2.** Sea-surface temperature anomalies in the Caribbean and surrounding region from 1982 to 2018 for month of September sea-surface temperatures (top-left). The red bar represents 2017 and the light blue bars represent El Nino years. (For interpretation of the references to color in this figure legend, the reader is referred to the Web version of this article.)

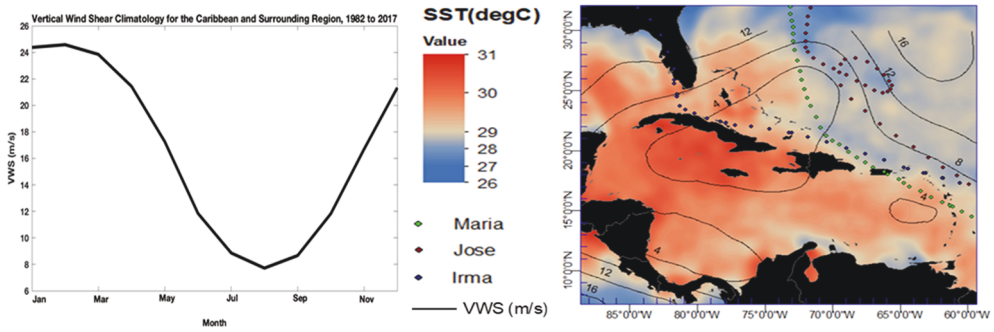


**Fig. 3.** VWS climatology for the Caribbean region (left) and SST, VWS contours and hurricane path (right) during September 2017.

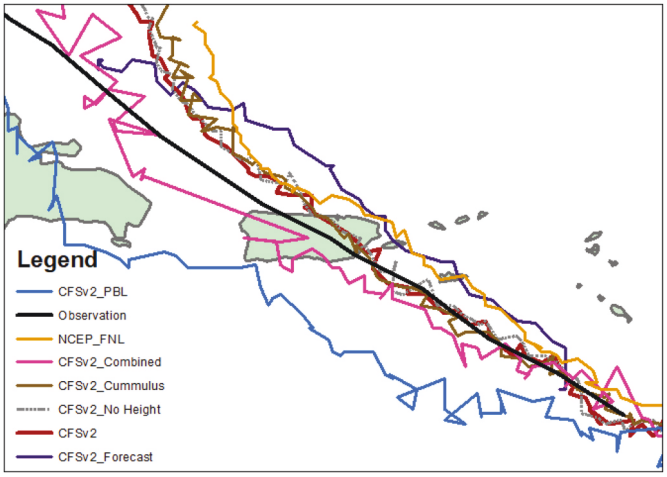


**Fig. 4.** Storm track representing minimum SLP.

a simulated and observed peak wind speed of 30 m/s on the southern coast. Model outputs are also compared with National Weather Service's (NWS) rainfall for the entire event. The interpolation of 63 different weather station data used by NWS is presented in Fig. 7 and is compared with WRF outputs. The Root Mean Square Error (RMSE) between WRF and NWS precipitation is 182 mm with a normalized RMSE of 0.2, which is minimum for CFSv2 as compared to other simulations. For both observation and model output, the maximum total precipitation is seen to be around the central mountain range with a magnitude of more than 640 mm.

The observed rainfall led to extreme streamflow conditions, which can be confirmed by using over 50 years of USGS stream gauge data for Puerto Rico. Given the variety of stream sizes, it is better to use normalization:

$$z_i = \frac{x_i - x_{min}}{x_{max} - x_{min}}$$

where $x_i$ is the stream gauge reading. This equation was used to normalize each station throughout its entire operational history starting from the 1950s and afterwards. Once this data was processed the mean of all the normalized stations was acquired and this was used to get an estimate of the average normalized flow of the waterways of the island. As it can be seen from the Fig. 8, Hurricane Maria was exceptional within our area of study period, whereas the second and third highest were for hurricane George (1998) and hurricane Irene (2011).

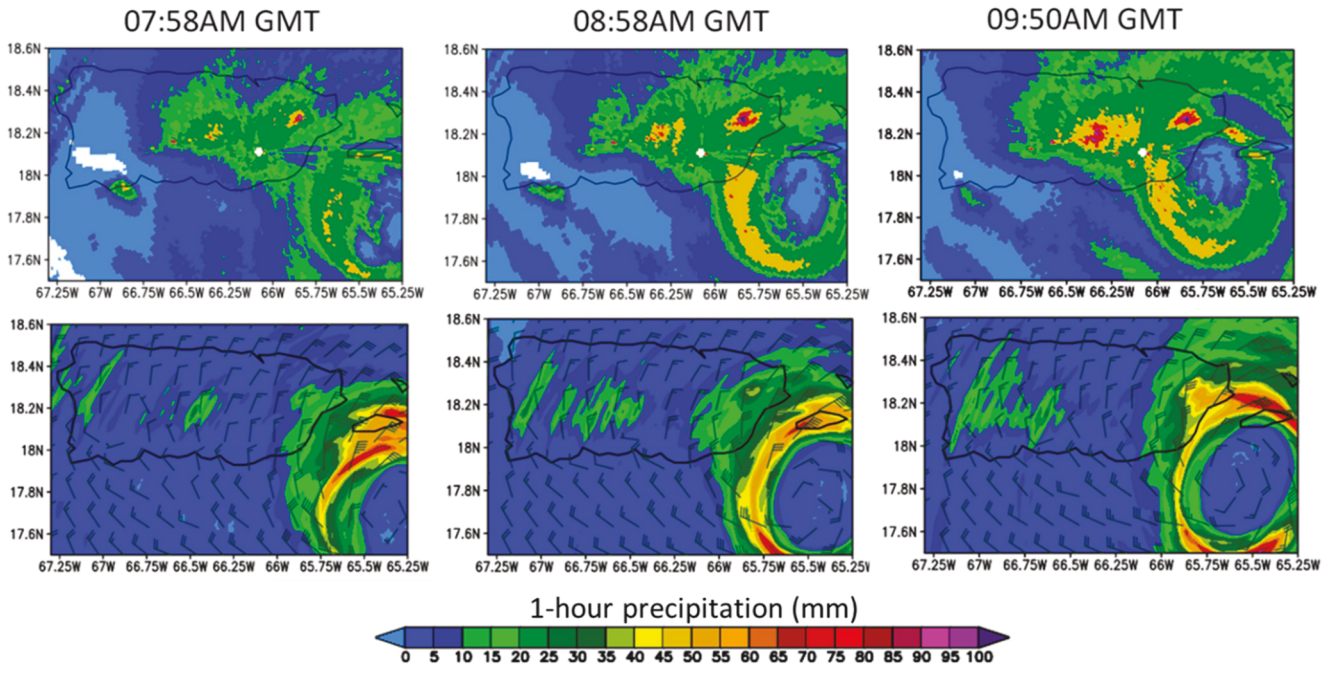


**Fig. 5.** Comparison of model results (bottom panel) with NEXRAD radar (top panel) for 1-h precipitation.

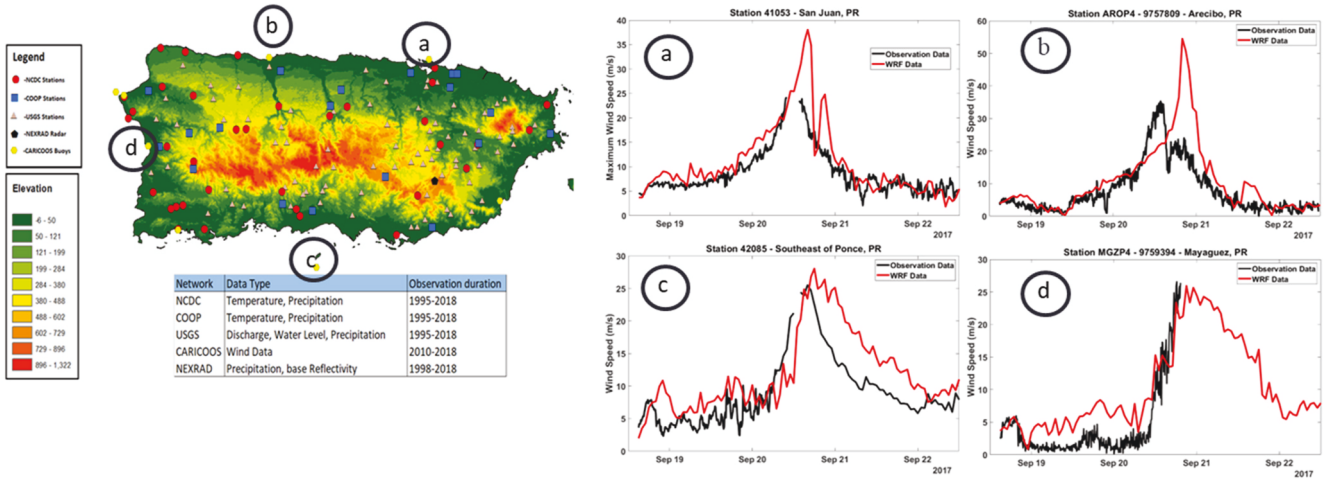


| Network | Data Type | Observation duration |
|---|---|---|
| NCDC | Temperature, Precipitation | 1995-2018 |
| COOP | Temperature, Precipitation | 1995-2018 |
| USGS | Discharge, Water Level, Precipitation | 1995-2018 |
| CARICOOS | Wind Data | 2010-2018 |
| NEXRAD | Precipitation, base Reflectivity | 1998-2018 |

**Fig. 6.** Wind observations from CARICOOS and model results at four coastal locations.

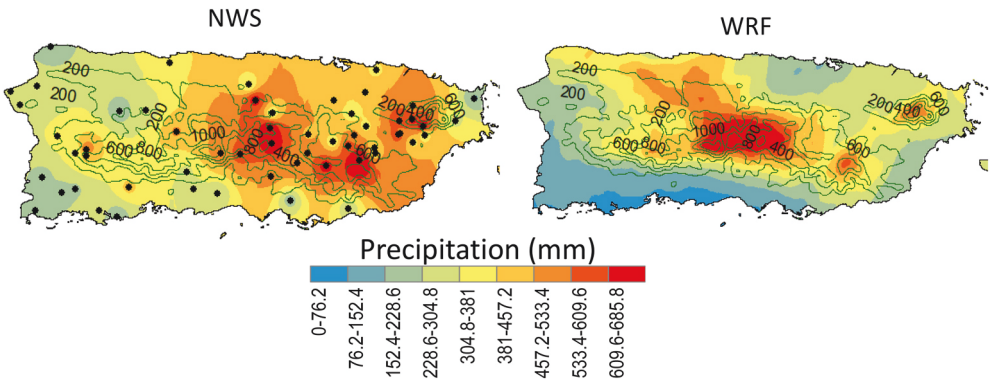


**Fig. 7.** NWS and WRF total precipitations (september 19–21, 2017).

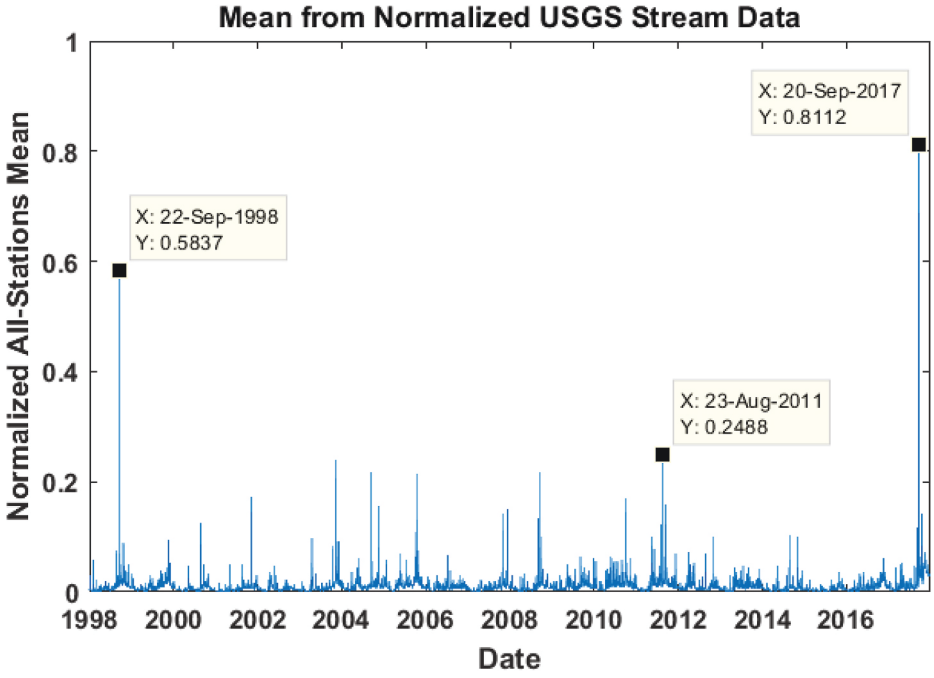


**Fig. 8.** Mean of Normalized Stream flow from 63 gauges. Dates from left to right are a) Hurricane George b) Hurricane Irene c) Hurricane Maria(USGS).

### 3.3. Precipitation and orographic effects from modeling results

Rainfall varies in a time-dependent fashion, even within a single precipitation event. The study of precipitation on a finer temporal scale, such as hourly rainfall, better reflects the essential physical characteristics of precipitation and is essential in many fields. Changes in the characteristics of short-term precipitation events are of interest because of the potential hydrologic impact of these events, including flash floods, erosion, landslides, debris flows, and urban water-logging (Ban et al., 2015; Zhang et al., 2011). Precise precipitation analysis based on sub-daily temporal data is therefore essential to accurately determine rainfall intensity, assess the related societal impacts, and understand the physical processes that drive precipitation during the event. Another critical parameter is Land Use and Land Cover (LULC), along with rainfall intensities that control the magnitude and frequency of overland flow and surface water erosion. Therefore, understanding the relationship between water and soil loss to extreme rainfall leads to relevant information on the management of land use and the conservation of soil and water. Surface runoff follows the seasonal distributions of precipitation patterns; peak during late rainfall season also the hurricane season on the island from August through November. For example, a study carried by the US Geological Service (USGS) on Lake Loiza (Gellis et al., 1999) which is a major water-supply reservoir for the capital city of San Juan, indicates that the amount of suspended sediment transported as a result of runoff produced by Hurricane Hugo, on September 18, 1989, for a 48-h transported less than half the suspended-sediment load that might have been expected from the amount of runoff for the whole year. The highest volume-weighted sediment concentration was measured at agricultural LCLU followed by pasture and forest. Lake Loiza has lost 47 percent of its capacity since impoundment in 1953. Brune curve analysis of historic bathymetric surveys indicates that it will be 90 percent filled by 2044. Evergreen broad leaf forest is a dominant LCLU in the entire island (Fig. 9 left) and the precipitation is seen to increase by 67% for the entire evergreen forest mainly due to the effect of orographic effect (Fig. 9 right). For instance, for LCLU-2 with elevation the total precipitation in 1.524 $km^3$ ($1524*10^6$ $m^3$) as compared to 0.9144 $km^3$ (914.4 $*10^6$ $m^3$ of water), i.e for LCLU the elevation enhanced the total precipitation by 67% for most common broad leaf forest for the island.

In order to geo-locate the impact of precipitation intensity, 6-h cumulative precipitation for different periods are represented with elevation in Fig. 10. The 6 hourly cumulative precipitation shows that the precipitation is as high as 254–305 mm for September 21_00 GMT to Sept 20_18 GMT, at the center and north-west of the Island. Thus, it is speculated that at this particular period, the region at center and northwest of the Island experienced rapid damage due to flooding and landslides and presented the ability to create more surface runoff and sediments. It is also noted that the central mountain range is exposed to rainfall for all periods.

In order to gain insights on the role of the orographic effects on event precipitation, it is necessary to analyze the vertical and horizontal wind speed over a central mountainous region. A cross-section of the region passing through 18.25°' latitude over the mountains along with horizontal wind speed in arrows and vertical wind speed in colored contours is presented in Fig. 11. The same section is also used to plot the rain water mixing ratios (the ratio of mass of liquid water to the mass of dry air in a unit volume of air; kg/kg) at various heights. It is noticed that high horizontal wind of 60–70 m/s creates a high upward vertical motion up-to 4 m/s (as seen in Sept20_18UTC), and high upward vertical motions produce high rain water mixing ratios along the same column, indicating more precipitation along those particular regions. The high upward vertical motion is clearly noticed over the mountainous regions were high horizontal wind speed is simulated.

Fig. 12 (a) presents the total storm rain water mixing ratio along the cross section that passes through Mayaguez (western coast) and the mountains range with simulation conducted with actual elevation and 12 (b) simulation conducted without elevation. Elevation along that cross section is also presented in Fig. 12 (a). The rain water mixing ratio is more pronounced along the mountains of Fig. 12 (a) compared with the sensitivity test without the elevation Fig. 12 (b). Fig. 12 (c) presents the cumulative event rainfall in mm without the elevations along with storm tracks. The result shows that the precipitation only follows the track when the orographic effect is neglected. There is not much difference in storm track for simulations with and without elevation however, the magnitude of total precipitation is much larger with actual elevation. Fig. 12 (d) presents the gain in event cumulative rainfall in percentage compared with rainfall without orographic effect. The presence of orographic variation along the center of the island (as shown by labeled contours lines at 250m contour interval) is simulated to enhance the precipitation by as high as four times as compared without elevations. In order to observe the orographic effects on other hurricanes, especially hurricane Irene (2011) and hurricane George (1998), an interpolation of various rain gauges for cumulative precipitation at different locations is presented in Fig. 13. It is observed that the central mountain range experiences more rainfall and is prone to landslides and damages due to flooding. The influence of topography in the climatological precipitation pattern of Puerto Rico is well documented (Daly et al., 2003; Comarazamy and González, 2008; Jury et al., 2009). Precipitation climatologically occurs when the easterly trade winds transport available moisture up the mountain slopes, acting as a lifting mechanism, forming a convergence zone atop the mountain ridge. This, in turn, leads to a high rain water mixing ratio along the columns, and consequently, surface accumulated precipitation (Comarazamy and González, 2011). The mean monthly precipitation records that precipitation slopes (average amount per kilometer of elevation) of 100–325 mm/km throughout the year with 299 mm/km during September. Orographic effects are shown to dominate the increase in mean precipitation by 100–150% over the island with the highest peaks occurring on the Cordillera Central and EL Yunque mountains (Daly et al., 2003).

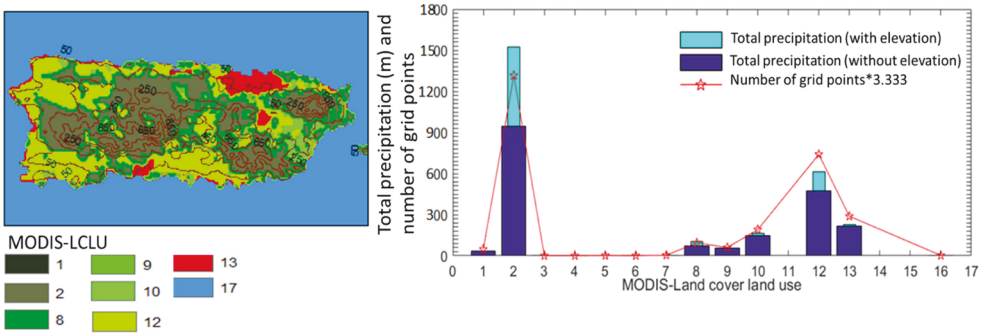


**Fig. 9.** MODIS, Land Cover Land Use (LCLU) with elevation (m) contours-:1-Evergreen Needleleaf Forest, 2-Evergreen Broadleaf Forest, 8-Woody Savannas, 9-Savannas, 10-Grasslands, 12-Croplands, 13-Urban and Built-Up. Total event precipitation with and without elevation on each LCLU including number of grids each at 1 km by 1 km resolution.

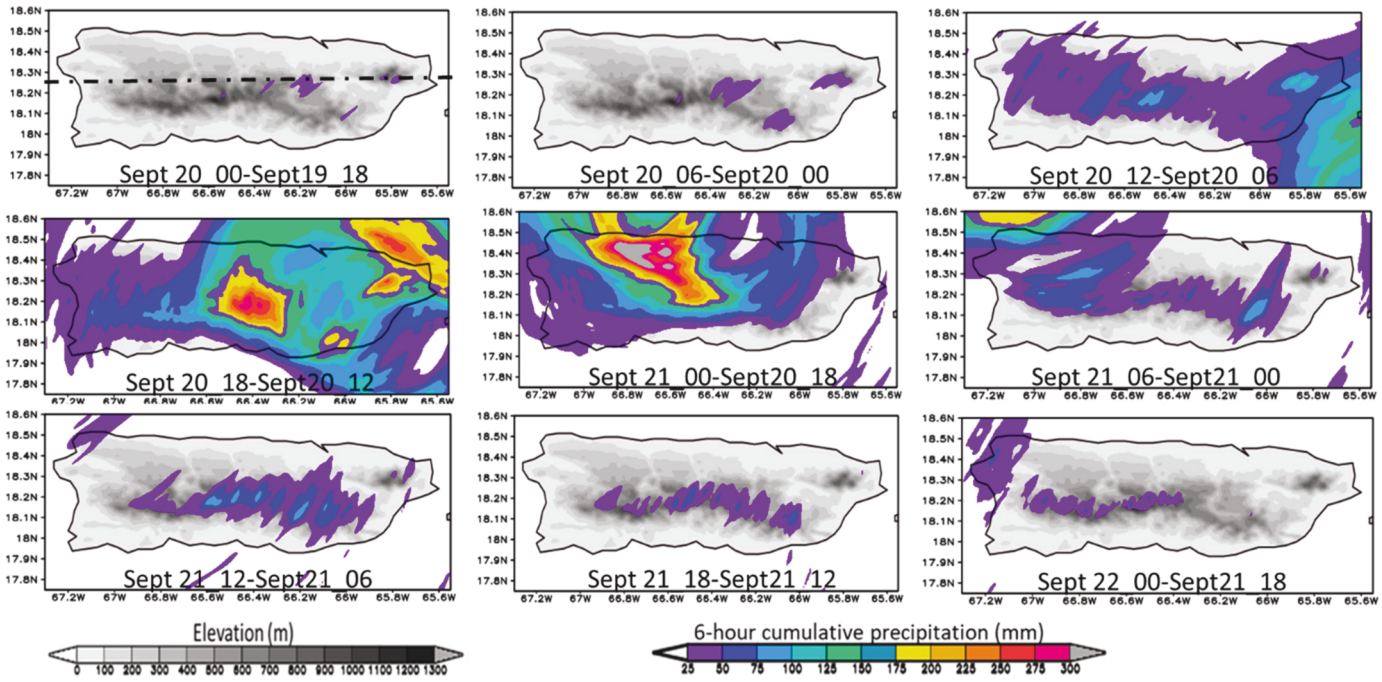


**Fig. 10.** 6-hourly cumulative precipitations during the event from September 20 to September 21.

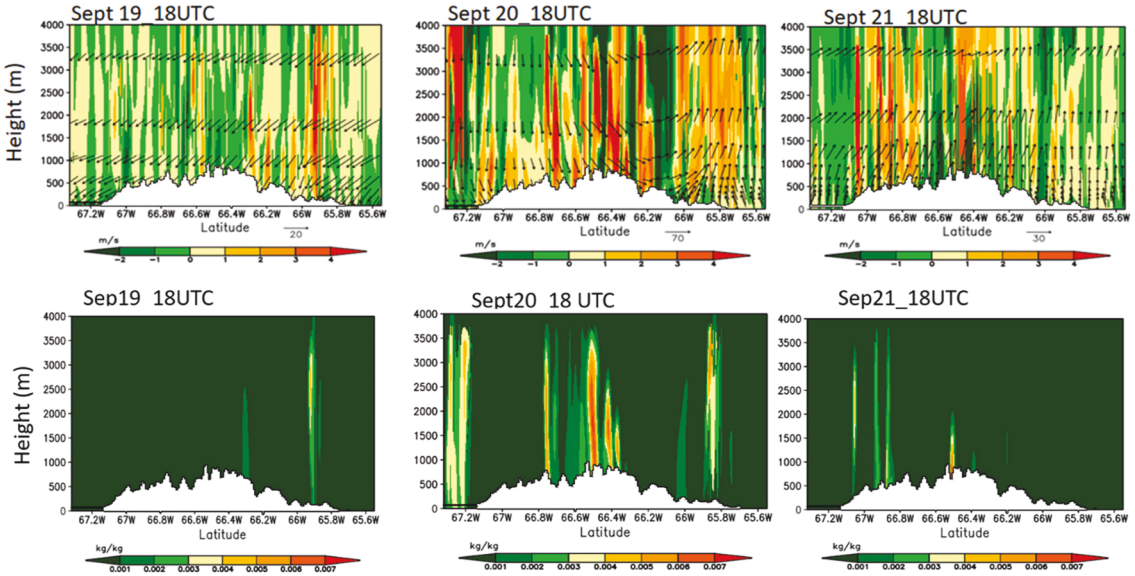


**Fig. 11.** Top panel represents a cross section passing through 18.25°' latitude with horizontal wind speed in arrow and vertical wind speed in colored contours. The bottom panel shows rain water mixing ratio for the same cross section.

Results of Fig. 12d, however, simulate a much higher increase in precipitation (300–400% increase) in the central mountain range mainly because of an extreme event as well as a combination of higher horizontal and upward vertical motion which controls the condensation rate and precipitation intensity, as well as the path of the storm being intercepted by the central mountain range.

### 3.4. Risk of failure of the electrical distribution poles

For the risk assessment on the electrical power infrastructure, the maximum wind speed per location during the event is used. The electrical power infrastructure was the most affected in the island generating cascading effects in the interconnected services of communications, water, and transportation (Pasch et al., 2018). On the left panel of Fig. 14, it is noticed that higher wind speeds occurred around the path of Hurricane, with values as high as 62–65 m/s in the north part of the path. The level of risk to failure can be estimated using mechanical failure stress analysis induced by high winds on electrical power poles (Keshavarzian 2003). This analysis is shown on the right panel of Fig. 14, where the high-risk areas (poles below class 4 will fail) are shown in red, the medium risk areas (poles below class 5 will fail) in yellow and the low-risk areas (none of the poles will fail) in green. The risk map shows high risk on the north part of the hurricane path, where the maximum wind speeds occurred. The high risks area is also noticed in the center of the island, where maximum precipitation is simulated.

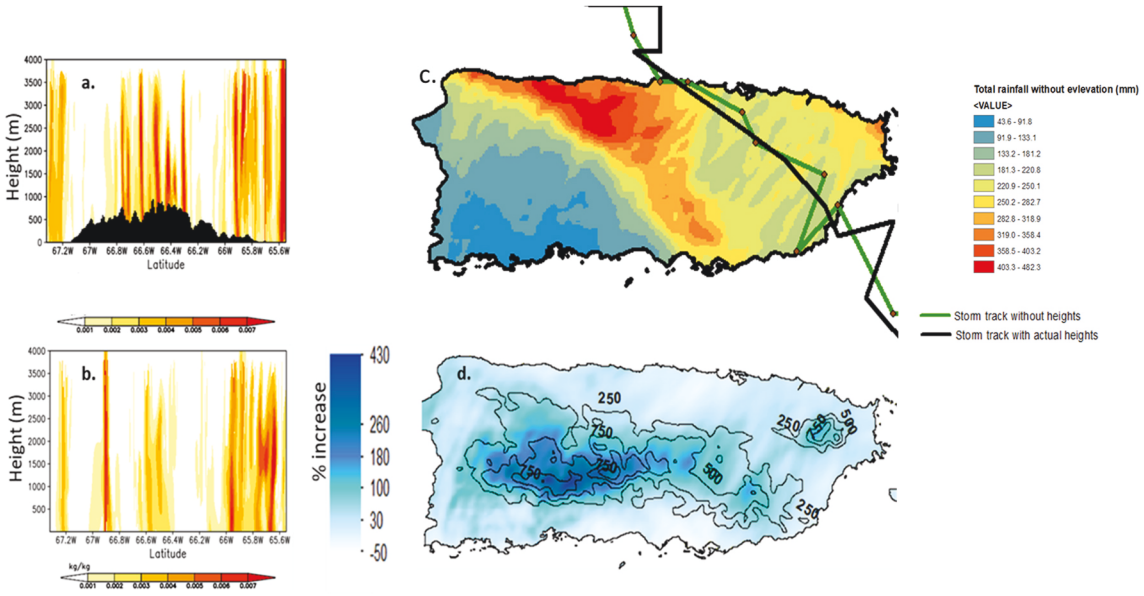


**Fig. 12.** (a) Rain water mixing ratio along the column with elevation (b) Rain water mixing ratio along the column without elevation, (c) Event cumulative rainfall (mm) without elevation along with storm tracks (d) event cumulative rainfall percentage increase as compared with without elevation.

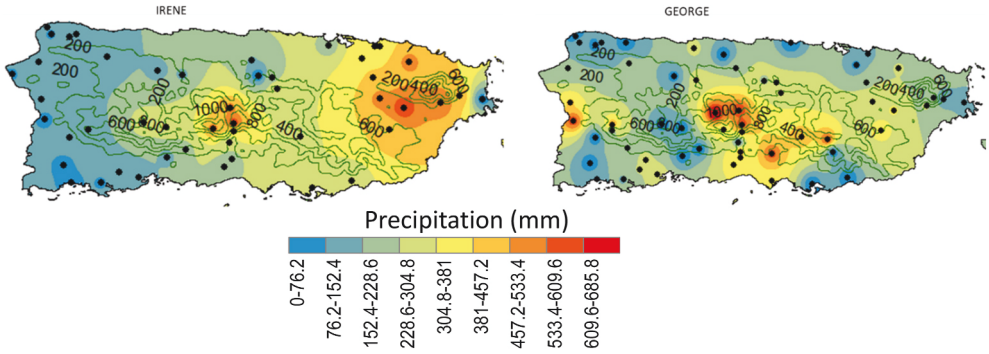


**Fig. 13.** Orographic effects observed in other storms.

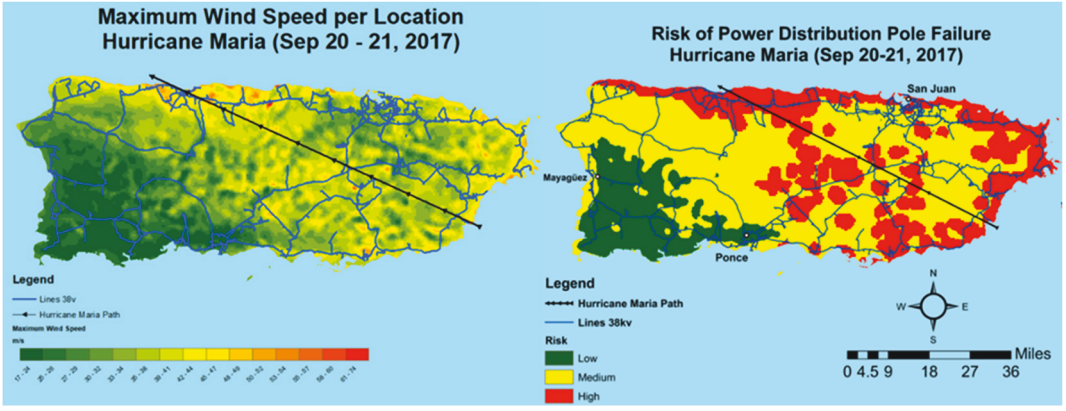


**Fig. 14.** Hurricane maria maximum wind speed and distribution poles risk of failure.

## 4. Conclusions

Modeling results have filled the information required when observation records have limited access to understand the physical phenomena relating to extreme weather events. The modeling effort provides us high spatial and temporal resolution for meteorological variables that provide physical insights and allow us to build sensitivity cases to answer critical questions that could be used for damage assessment. Hurricane Maria was an exceptional storm with record-high mortality and infrastructure damage in the Island of Puerto Rico. The study's motivation is to provide insights before and during the event for impact analysis, especially on critical power infrastructure. This work recreates

the geophysical conditions that led to the storm during its passage across the Island using mesoscale weather models (WRF) for a limited ensemble arrangement that considers input variables and physical parameterizations. The ensemble results are compared with limited observational records for this particular extraordinary event. Our synoptic analysis of conditions that led to the storm indicate record high SSTs and low vertical wind shear during September 2017, which fed to the storm causing historic high precipitation and stream flows. The model results compare well with the limited observational records available for wind speed and are also validated for the rainfall in the entire Island with a normalized RMSE of 0.2. Results also demonstrate that high horizontal wind produces a high upward vertical motion at the central mountain range of the Island with peaks above 1300 m, enhancing convection that eventually produces high rain water mixing ratios along the same column, thereby increasing the total precipitation. It is also simulated that the orographic variation enhances the rainfall by more than four times along the central mountains as the storm passes through the same region. As an example of damage assessment due to extreme wind, a simplified risk of failure analysis of the electric distribution poles is carried out. The results demonstrate that high risk of electric poles' failure occurred at the north and center of the Island where high wind speed and high precipitation are simulated. The validated meteorological variables can be further utilized for further impact assessments such as hydrological modeling (for flood risk) and resiliency model (for impact on critical infrastructures). Future works will be focused on generating reliable data sources for other hurricanes in the Island and utilizing the data for impacts on critical infrastructures.

## Declaration of competing interest

The authors declare that they have no known competing financial interests or personal relationships that could have appeared to influence the work reported in this paper.

## Acknowledgements

The authors would like to acknowledge the assistance and suggestions from members of the Coastal Urban Environmental Research Group from City College New York and of the University of Puerto Rico Mayaguez. The analysis process was conducted at the high performance computing facilities at City College of New York (http://cuerg.ccny.cuny.edu/), the College of Staten Island CUNY, High Performance Computing Center (https://cunyhpc.csi.cuny.edu/) and the National Center for Atmospheric Research (NCAR) supercomputers. Financial support for this research was provided by the US National Science Foundation (Award No CBET-1438324 & Award No.1832678).

## References

Ban, N., Schmidli, J., Schär, C., 2015. Heavy precipitation in a changing climate: does short-term summer precipitation increase faster? Geophys. Res. Lett. 42, 1165–1172. https://doi.org/10.1002/2014gl062588.

Bjarnadottir, S., Li, Y., Stewart, M.G., 2013. Hurricane risk assessment of power distribution poles considering impacts of a changing climate. J. Infrastruct. Syst. 19 (1), 12–24. https://doi.org/10.1061/(ASCE)IS.1943-555X.0000108.

Boose, E.R., Serrano, M.I., Foster, D.R., 2004. Landscape and regional impacts of hurricanes in Puerto Rico. Ecol. Monogr. 74 (2), 335–352. https://doi.org/10.1890/02-4057.

Comarazamy, D.E., Gonzalez, J.E., Andreopoulos, Y., 2020. Projections of wind gusts for New York city under a changing climate. ASME.J. Eng.Sustain.Build.Cities 1 (3), 1–13. https://doi.org/10.1115/1.4048059.

Comarazamy, D.E., González, J.E., 2011. Regional long-term climate change (1950-2000) in the midtropical Atlantic and its impacts on the hydrological cycle of Puerto Rico. J. Geophys. Res. Atmos. 116 (12), 1–18.

Comarazamy, D.E., González, J.E., 2008. On the validation of the simulation of early season precipitation on the island of Puerto Rico using a mesoscale atmospheric model. J. Hydrometeorol. 9, 507–520. https://doi.org/10.1175/2007JHM804.1.

Chelliah, M., Bell, G.D., 2004. Tropical multidecadal and interannual climate variability in the NCEP–NCAR reanalysis. J. Clim. 17, 1777. https://doi.org/10.1175/1520-0442(2004)017<1777:TMAICV>2.0.CO;2.

Chen, H., Zhang, D.L., Carton, J., Atlas, R., 2011. On the rapid intensification of Hurricane Wilma (2005). Part I: model prediction and structural changes. Weather Forecast. 26, 885–901. https://doi.org/10.1175/WAF-D-11-00001.1.

Colón-pagán, I.C., 2009. Orographic Effects on Rainfall Induced by the Passage of Tropical Cyclones over Mountainous Islands : 1–25.

Daly, C., Helmer, E.H., Quiñones, M., 2003. Mapping the climate of Puerto Rico, Vieques and Culebra. Int. J. Climatol. 23, 1359–1381. https://doi.org/10.1002/joc.93.

Davis, C.A., Jones, S.C., Riemer, M., 2008. Hurricane vortex dynamics during Atlantic extratropical transition. J. Atmos. Sci. 65, 714–736. https://doi.org/10.1175/2007JAS2488.1.

Dudhia, J., 1989. Numerical study of convection observed during the winter monsoon experiment using a mesoscale two-dimensional model. J. Atmos. Sci. 46 (20), 3077–3107, 1989.

Emanuel, K.A., 1999. Thermodynamic control of hurricane intensity. Nature 401, 665.

Puerto Rico Aqueduct and Sewer Authority., and Geological Survey (U.S.) Gellis, A.C., 1999. Effects of land use on upland erosion, sediment transport, and reservoir sedimentation, Lago Loíza Basin, Puerto Rico. Water-resources Investig. Rep. 99–4010, 60. vii.

Glenn, E., Comarazamy, D., González, J.E., Smith, T., 2015. Detection of recent regional sea surface temperature warming in the Caribbean and surrounding region. Geophys. Res. Lett. 42, 6785–6792. https://doi.org/10.1002/2015GL065002.

Gray, W.M., 1984. Atlantic seasonal hurricane frequency. Part I: El Niño and 30 mb quasi-Biennial oscillation influences. Mon. Weather Rev. 112, 1649. https://doi.org/10.1175/1520-0493(1984)112<1649:ASHFPI>2.0.CO;2.

Henderson-Sellers, A., et al., 1998. Tropical cyclones and global climate change: a post-IPCC assessment. Bull. Am. Meteorol. Soc. 79, 19. https://doi.org/10.1175/1520-0477(1998)079<0019:TCAGCC>2.0.CO;2.

Holland, G.J., 1997. The maximum potential intensity of tropical cyclones. J. Atmos. Sci. 54, 2519–2541. https://doi.org/10.1175/1520-0469(1997)054<2519:TMPIOT>2.0.CO;2.

Hong, S., Lim, J., 2006. The WRF single-moment 6-class microphysics scheme (WSM6). J.Kor.Meteorol. Soc 42 (2), 129–151.

Hong, S.-Y., Yign, N., Dudhia, J., 2006. A new vertical diffusion package with an explicit treatment of entrainment processes. Mon. Weather Rev. 134, 2318–2341. https://doi.org/10.1175/MWR3199.1.

Hosannah, N., Ramamurthy, P., Marti, J., Munoz, J., Gonzalez, J.E., 2020. Impacts of Hurricane Maria on Land and Convection Modification over Puerto Rico. JGR Atmospheres. https://doi.org/10.1029/2020JD032493.

Jury, M.R., 2011. Long-term variability and trends in the Caribbean Sea, 2011 Int. J. Oceans 9. Article ID 465810.

Jury, M.R., Chiao, S., Harmsen, E.W., 2009. Mesoscale structure of trade wind convection over Puerto Rico: Composite observations and numerical simulation. Boundary-Layer Meteorol. 132, 289–313. https://doi.org/10.1007/s10546-009-9393-3.

Kain, J.S., 2004. The kain–Fritsch convective parameterization: an update. J. Appl. Meteorol. 43 (1), 170–181.

Kalnay, et al., 1996. The NCEP/NCAR 40-year reanalysis project. Bull. Am. Meteorol. Soc. 77, 437–470.

Karim, M.F., Mimura, N., 2008. Impacts of climate change and sea-level rise on cyclonic storm surge floods in Bangladesh. Global Environ. Change 18 (3), 490–500. https://doi.org/10.1016/j.gloenvcha.2008.05.002.

Keellings, D., Hernández Ayala, J.J., 2019. Extreme rainfall associated with Hurricane Maria over Puerto Rico and its connections to climate variability and change. Geophys. Res. Lett. 46, 2964–2973. https://doi.org/10.1029/2019GL082077.

Keshavarzian, M., 2003. Extreme wind design of self-supported steel structure: critical review of related ASCE publications. Pract. Period. Struct. Des. Construct. 8 (2), 102–106.

Khain, A., Lynn, B., Dudhia, J., 2010. Aerosol effects on intensity of landfalling hurricanes as seen from simulations with the WRF Model with spectral bin microphysics. J. Atmos. Sci. 67, 365–384. https://doi.org/10.1175/2009JAS3210.1.

Kishore, N., Marqués, D., Mahmud, A., Kiang, M.V., Rodriguez, I., Fuller, A., et al., 2018. Mortality in Puerto Rico after hurricane Maria. N. Engl. J. Med. 379 (2), 162–170. https://doi.org/10.1056/NEJMsa1803972.

Lin, N., Emanuel, K.A., Smith, J.A., Vanmarcke, E., 2010a. Risk assessment of hurricane storm surge for New York City. J. Geophys. Res. Atmos. 115 (18), 1–11. https://doi.org/10.1029/2009JD013630.

Lin, Ning, Smith, J.A., Villarini, G., Marchok, T.P., Baeck, M.L., 2010b. Modeling extreme rainfall, winds, and surge from hurricane isabel (2003). Weather Forecast. 25 (5), 1342–1361. https://doi.org/10.1175/2010WAF2222349.1.

Mann, M.E., Emanuel, K.A., 2006. Atlantic hurricane trends linked to climate change. Eos 87 (24), 233. https://doi.org/10.1029/2006EO240001.

Moon, Y., Nolan, D.S., 2015. Spiral rainbands in a numerical simulation of Hurricane Bill (2009). Part I: structures and comparisons to observations. J. Atmos. Sci. 72, 164–190. https://doi.org/10.1175/JAS-D-14-0058.1.

Mlawer, E.J., Taubman, S.J., Brown, P.D., Iacono, M.J., Clough, S.A., 1997. Radiative transfer for inhomogeneous atmospheres: RRTM, a validated correlated-k model for the longwave. J. Geophys. Res. Atmos. 102 (D14), 16663–16682.

Mudd, L., Wang, Y., Letchford, C., Rosowsky, D., 2014. Hurricane wind hazard assessment for a rapidly warming climate scenario. J. Wind Eng. Ind. Aerod. 133, 242–249. https://doi.org/10.1016/j.jweia.2014.07.005.

National Hurricane Center (NHC) report on Tropical Cyclone, 2019. Hurricane Maria. Hurricane Maria (noaa.gov).

NOAA National Centers for Environmental Information, 2017. State of the Climate: Global Climate Report for Annual published online January 2018, retrieved on September 17, 2019 from. https://www.ncdc.noaa.gov/sotc/global/201713.

Panteli, M., Pickering, C., Wilkinson, S., Dawson, R., Mancarella, P., 2017. Power system resilience to extreme weather: Fragility modeling, probabilistic impact assessment, and adaptation measures. IEEE Trans. Power Syst. 32 (5), 3747–3757. https://doi.org/10.1109/TPWRS.2016.2641463.

Pasch, R., Penny, A., Berg, R., 2018. Tropical Cyclone Report Hurricane Maria (AL152017). Miami, FL.

Paterson, L.A., Hanstrum, B.N., Davidson, N.E., Weber, H.C., 2005. Influence of environmental vertical wind shear on the intensity of hurricane-strength tropical cyclones in the Australian region. Mon. Weather Rev. 133, 3644–3660.

Patricola, C.M., Wehner, M.F., 2018. Anthropogenic influences on major tropical cyclone events. Nature 563 (7731), 339–346. https://doi.org/10.1038/s41586-018-0673-2.

Philpott, S.M., Lin, B.B., Jha, S., Brines, S.J., 2008. A multi-scale assessment of hurricane impacts on agricultural landscapes based on land use and topographic features. Agric. Ecosyst. Environ. 128 (1–2), 12–20. https://doi.org/10.1016/j.agee.2008.04.016.

Pielke, R.A., Rubiera, J., Landsea, C., Fernández, M.L., Klein, R., 2003. Hurricane vulnerability in Latin America and the Caribbean: normalized damage and loss potentials. Nat. Hazards Rev. 4 (3), 101–114. https://doi.org/10.1061/(ASCE)1527-6988(2003) 4:3(101).

Reynolds, R.W., Smith, T.M., Liu, C., Chelton, D.B., Casey, K.S., Schlax, M.G., 2007. Daily high-resolution blended analyses for sea surface temperature. J. Clim. 20, 5473–5496.

Saha, S., et al., 2014. The NCEP climate forecast system version 2. J. Clim. 27, 2185–2208. https://doi.org/10.1175/JCLI-D-12-00823.1.

Skamarock, W.C., et al., 2008. A description of the advanced research WRF version 3. Tech. Rep., no. June 113.

Tang, B.H., Neelin, J.D., 2004. ENSO Influence on Atlantic hurricanes via tropospheric warming. Geophys. Res. Lett. 31, L24204. https://doi.org/10.1029/2004GL021072.

Tewari, M., Chen, F., Wang, W., Dudhia, J., LeMone, M., Mitchell, K., Ek, M., Gayno, G., Wegiel, J., Cuenca, R., 2004. Implementation and Verification of the unified NOAH land surface model in the WRF model. In: 20th Conference on Weather Analysis and Forecasting/16th Conference on Numerical Weather Prediction, pp. 11–15. Seattle, WA, Jan 10-15.

Zhang, H., Zhai, P.M., 2011. Temporal and spatial characteristics of extreme hourly precipitation over eastern China in the warm season. Adv. Atmos. Sci. 28, 1177–1183. https://doi.org/10.1007/s00376011-0020-0, 2011.

Zhang, W., Villarini, G., Vecchi, G.A., Smith, J.A., 2018. Urbanization exacerbated the rainfall and flooding caused by hurricane Harvey in Houston. Nature 563 (7731), 384–388. https://doi.org/10.1038/s41586-018-0676-z.